Sub-ppm gas phase Raman spectroscopy in an anti-resonant hollow core fiber

THOMAS W. KELLY,[1,]* IAN A. DAVIDSON,[1] CHARLES WARREN,[2] WILLIAM S. M. BROOKS,[2] MICHAEL J. FOSTER,[2] FRANCESCO POLETTI,[1] DAVID J. RICHARDSON,[1] PETER HORAK,[1] AND NATALIE V. WHEELER[1]

[1] *Optoelectronics Research Centre, University of Southampton, SO17 1BJ, United Kingdom*
[2] *IS-Instruments Ltd., 220 Vale Road, Tonbridge, Kent TN9 1SP, United Kingdom*
*twk1g15@soton.ac.uk

Abstract: We demonstrate recent progress in the development of a Raman gas sensor using a single cladding ring anti-resonant hollow core micro-structured optical fiber (HC-ARF) and a low power pump source. The HC-ARF was designed specifically for low attenuation and wide bandwidth in the visible spectral region and provided low loss at both the pump wavelength (532 nm) and Stokes wavelengths up to a Raman shift of $5000\,cm^{-1}$. A novel selective core pressurization scheme was also implemented to further reduce the confinement loss, improving the Raman signal enhancement by a factor of 1.9 compared to a standard fiber filling scheme. By exploiting longer lengths of fiber, direct detection of both methane and hydrogen at concentrations of 5 and 10 ppm respectively is demonstrated and a noise equivalent limit-of-detection of 0.15 ppm is calculated for methane.

1. Introduction

Highly sensitive gas sensors are required for applications in medical diagnostics, industrial processing, and environmental sensing. Many sensors are electro-chemical [1], for example those that are semiconductor based, such as metal oxide gas sensors [2]. While these sensors are low in cost, have high analytical sensitivity, and offer fast response times, they offer poor selectivity and as a result suffer from cross sensitivity. Gas chromatography (GC), often used for the separation of volatile organic compounds (VOCs) and coupled with mass spectrometers or flame ionization detectors, is commonly used in industry [3]. Although this technique allows for the analysis of complex mixtures in trace amounts, prior knowledge of the sample is required, often involving pre-preparation steps. Furthermore, GC is often bulky and expensive. Optical methods, being fast and potentially highly specific, are well suited for gas sensing applications. Narrowband tunable diode laser absorption spectroscopy (TDLAS) [4], photoacoustic spectroscopy, and broadband Fourier transform infrared spectroscopy (FTIR) are a few examples [5]. While these infrared-absorption based techniques offer excellent selectivity and analytical sensitivity they are usually optimized for single-species detection or cannot detect homonuclear gases such as nitrogen, oxygen and hydrogen which are highly relevant for a wide range of applications including the environmental sciences, for monitoring of hydrogen as an alternative energy source in the gas supply [6] as well as for isotopic discrimination of hydrogen, deuterium (^{2}H) and tritium (^{3}H) in the nuclear industry [7]. Moreover, water has very prominent broad absorption features in the infrared which can mask the absorption features of other gases to be analyzed.

Raman spectroscopy (based on spontaneous Raman scattering) is a highly selective technique, whereby vibrational peaks and rotational bands provide a unique spectral signature which enables

analysis of a complex, multispecies gas mixture using a single monochromatic pump source. However, the small scattering cross sections of gases (of the order 10^{-27} cm^2) mean that the probability of observing an inelastic Raman scatter is orders of magnitude less than that of an elastic (Rayleigh) scatter [8]. This means that the generated Raman light is very weak and therefore resonant optical cavities or multi-pass cells consisting of highly reflective mirrors are necessary to increase the gas-light interaction length and to achieve a sufficient limit-of detection (LoD) for gas sensing applications in the ppm or sub-ppm range [9,10]

Confining the gas sample under test within a hollow core microstructured optical fiber (HC-MOF) has been shown to be a very promising alternative approach for increasing the gas-light interaction length for sensing applications and beyond [11]. In this scenario, the fiber can act as a compact and lightweight sampling cell in optical spectroscopic systems or enable remote gas detection from hazardous locations. Several laser-based spectroscopy techniques have been explored for ultra-sensitive gas detection with HC-MOFs: a novel mode-phase-difference photothermal spectroscopy technique demonstrating a noise-equivalent detection limit for acetylene in the parts-per-trillion (ppt) range [12,13], photoacoustic Brillouin spectroscopy, where absorption of the gas excites acoustic resonances within the fiber demonstrating detection of acetylene at parts-per-billion (ppb) levels [14], and also wavelength modulation spectroscopy, where recently a minimum detection limit of 670 ppt over a 30 m length of mid-IR guiding fiber was reported for ethane [15], to name but a few. While ultra-sensitive detection of single species has been achieved using these techniques, the complexity greatly increases for multi-component analysis, requiring multiple laser sources each tuned to a specific absorption line.

Buric *et al.* first proposed using a hollow-core photonic bandgap fiber (PBGF) for enhanced spontaneous gas phase Raman spectroscopy and demonstrated over 100 times enhancement over a standard free-space configuration [16,17]. Hanf *et al.* also demonstrated simultaneous detection of H_2 and CH_4 as well as other relevant gases using a PBGF in the context of breath analysis for early-stage diagnosis of various metabolic disorders, demonstrating a LoD of 4.7 ppm for hydrogen [18,19]. A similar study was also done by Chow *et al.* [20]. Limits of detection as low as 0.2 ppm for methane and 9 ppm for nitrogen have been reported using a PBGF, although at a high pump power and gas pressure (2 W and 20 bar respectively) [19].

Hollow core anti-resonant fibers (HC-ARFs) are a second class of HCF which guide by a combination of anti-resonance and inhibited coupling. Here, a series of glass membranes of equal thickness surround a hollow core region. A sub-class are the single-cladding ring ("tubular" or "revolver" [21–23]) type, where a series of non-contacting thin tubular membranes attached to the fiber jacket surround a central core region. The negative curvature boundary surrounding this core mitigates issues relating to undesired resonances within the otherwise smooth, broad bandwidth transmission windows by ensuring that any thicker glass nodes (such as where the cladding tubes meet the jacket) are as far away from the core as possible. HC-ARFs offer several advantages for Raman gas sensing as compared to PBGFs, including larger core diameters (faster pressure-driven gas ingress), lower light-glass overlap (reduced Raman background generated within the silica microstructure), lower losses in the visible and wider wavelength transmission ranges [24]. Recently, detection of $^{13}CO_2$, $^{12}CO_2$, $^{18}O_2$ and $^{16}O_2$ in a single measurement was demonstrated using a single-cladding ring tubular fiber in the context of isotopic labelling experiments [25]. However, up until now, the LoD demonstrated using HC-ARFs for Raman-based gas sensing has not reached the sub-ppm level achieved with PBGFs due to the lower numerical aperture and thus lower capture efficiency of HC-ARFs.

2. Methods

The experimental configuration of our HCF-based Raman gas sensor is shown in Fig. 1. A CW Coherent Sapphire optically pumped semiconductor laser (OPSL) operating at a wavelength of 532 nm (maximum output power 150 mW) was used as the pump source. Light was coupled

into the HC-ARF via a dichroic mirror (DM, Semrock) and an aspheric lens (L2, Thorlabs 220TMD-A, f = 11.00 mm, NA = 0.25, beam spot size at the focus: ∼ 9.9 μm). A power meter (PM) at the distal end of the fiber provides a means to measure the coupling efficiency and optimize optical alignment. We estimate a coupling efficiency in our experiment of 84% into the fundamental mode. The HC-ARF is mounted on a v-groove that sits on a 3-axis NanoMax flexure stage (Thorlabs). Stokes light generated within the fiber is then collimated by L2 and passes through a variable iris inserted between the DM and L2 [26]; the iris aperture size is carefully adjusted to a diameter of ∼0.8 mm to optimize the signal-to-noise ratio (SNR). While in an AR-HCF the Raman signal which originates from the silica microstructured cladding is significantly reduced as compared to a PBGF, the variable iris between the DM and L2 can be used as a means to spatially filter any unwanted scattered light which is generated within the launch optics and at the fiber input. The backscattered Raman signal then passes through the DM, and a 532 nm edge filter (Semrock) to suppress any Rayleigh scattered light before being re-focused into a multi-mode fiber (MMF) by a second aspheric lens (L1, Thorlabs 280TMD-A, f = 18.40 mm, NA = 0.15) which couples the light into a dispersive spectrometer for analysis. The spectrometer is in a Czerny-Turner configuration and contains a holographic grating (1800 lines/mm Thorlabs) configured to measure between 2252 cm^{-1} and 4464 cm^{-1} with a resolution of ∼0.8 cm^{-1}. The spectrometer is equipped with an Andor iVac324 200 × 1650 CCD camera cooled to ∼−60°C.
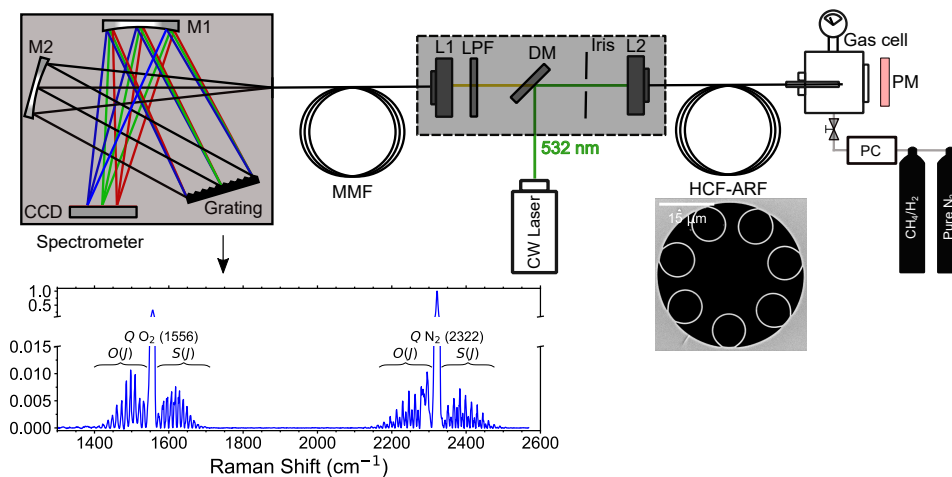

Fig. 1. Experimental setup for gas phase Raman measurements. DM = dichroic mirror; L1 & L2 = aspheric lens; LPF = long-pass filter; MMF = multimode fiber; PC = pressure controller.

Pre-mixed gas samples (BOC) are delivered to the distal end of the HCF pressure controller (PC, Mensor CPC4000) with the setpoint fixed at 5 bar gauge pressure. Gases emerging from the output side of the PC are fed into a stainless-steel gas cell fabricated in-house and equipped with a pressure gauge. The cell interfaces with the distal end of the fiber to allow for gas filling and has an incorporated optical window so the pump throughput power can be measured.

For all measurements reported in this manuscript, a series of spectra were acquired and averaged to reduce noise, then subsequently underwent background subtraction, flat field correction (to account for variations in CCD overall instrument pixel-to-pixel sensitivity) and then baseline fitting and removal. Figure 1 (inset lower left) shows a Raman spectrum from a 3.4 m length of fiber after being purged with zero-grade air (ultra-pure synthetic air supplied by BOC 19.9-21.9% oxygen with nitrogen balance), for an integration time of 5 s. The weak $O_1(J)$ and $S_1(J)$ branches

(corresponding to various ro-vibrational transitions) can be resolved above the noise floor on either side of the central Q_1-branch.

As mentioned in Section 1, one drawback of using a HC-ARF is the low numerical aperture of these fibers (NA ~ 0.03 for specific fibers used in this work). The Raman capture efficiency of the system is strongly dependent on the $L\Omega$ product, where L is the interaction length and Ω the solid angle of the Raman acceptance cone [16]. The angular acceptance of the fiber, θ, can be estimated from the NA by: $\sin^{-1}(\text{NA})$. Since θ is small, $\Omega \approx \pi\theta^2$ and it follows that $\Omega \approx 0.0028$ sr. A commercially available visible 7-cell PBGF has an NA of the order ~ 0.12 [27], and therefore an acceptance cone with a solid angle approximately 11 times that of the tubular HC-ARF. The small acceptance cone however is compensated by the lower transmission loss of tubular type HC-ARF compared to an equivalent 7-cell visible PBGF [27] allowing long lengths of fiber to be used, thus increasing L. The larger core sizes and mode-field diameters of HC-ARFs allow for faster gas exchange compared to PBGFs, and greater tolerances to drift in coupling alignment.

3. GDRI in HCFs

The fiber used in this work has a minimum loss of 35.9 dB/km at 619 nm and was fabricated by the conventional stack and draw process; further details can be found in [28]. A scanning electron microscope (SEM) image of the fiber cross-section is shown in Fig. 2(a); it has a core diameter of 20.5 ± 0.2 µm, inter-tube gap of 3.5 ± 0.4 µm, and an average membrane thickness of 440 ± 10 nm. The fiber was designed to operate in the second (visible) transmission window which encompasses the pump at 532 nm up to the vibrational hydrogen shift at ~ 680 nm covering the Raman Stokes signals of all key gases. It is robust against bending (0.1 dB/m, 16 cm bend diameter, 532 nm) [28], which is beneficial in this application where long lengths are used as a compact footprint is possible. Also, Fig. 2(b) shows a far field beam profile of the fiber's fundamental mode.

We recently demonstrated that introducing a gas-induced differential refractive index (GDRI) between the gas within the core and cladding regions of a HC-ARF enables dramatic changes to the fiber's optical properties [29,30]. Specifically, we showed that by selectively increasing the core gas pressure (while keeping the gas in the cladding holes at atmospheric pressure) can significantly reduce the confinement loss. Experimentally, this selective gas filling was achieved by collapsing the cladding tubes using an arc–fusion splicer at the point of the gas inlet (in our case at the distal end of the fiber). Upon heating the fiber, the smaller cladding holes collapse faster than the core (due to surface tension) and the heating parameters can be controlled such that the core remains open while the cladding holes collapse. The microstructure tapers outwards from the collapse point which forms a waist. Cleaving at the taper waist results in the end-facet of the fiber being exposed with an open core and sealed capillary tubes. The same technique is applied in this work for selective core gas-filling measurements.

The lower panel of Fig. 2(c) compares the normalized fundamental mode power at 532 nm with the core filled with 1 bar and 6 bar (absolute pressure) nitrogen along the horizontal plane $y = 0$ which passes through the centre of an adjacent capillary (cladding gas pressure at 1 bar in both cases). When comparing the power at the inner jacket boundary within the right-hand side capillary with the core pressure raised to 6 bar (blue curve), it is around 20 dB below the power with the core at 1 bar (red curve), leading to a reduction in confinement loss. This is confirmed in Fig. 2(d) which shows the confinement loss in the visible with the core pressure raised (blue trace) and at 1 bar (red trace). For the previously described modelling, and to match the experimental conditions used in this paper, the distal end of a 12 m length of fiber is at a pressure of 6 bar, the proximal end at 1 bar resulting in a 5-bar differential pressure. The loss along the entire fiber length is found by integrating over the pressure distribution established along the fiber core due to this differential [29]. The fiber loss (measured by cutback technique)
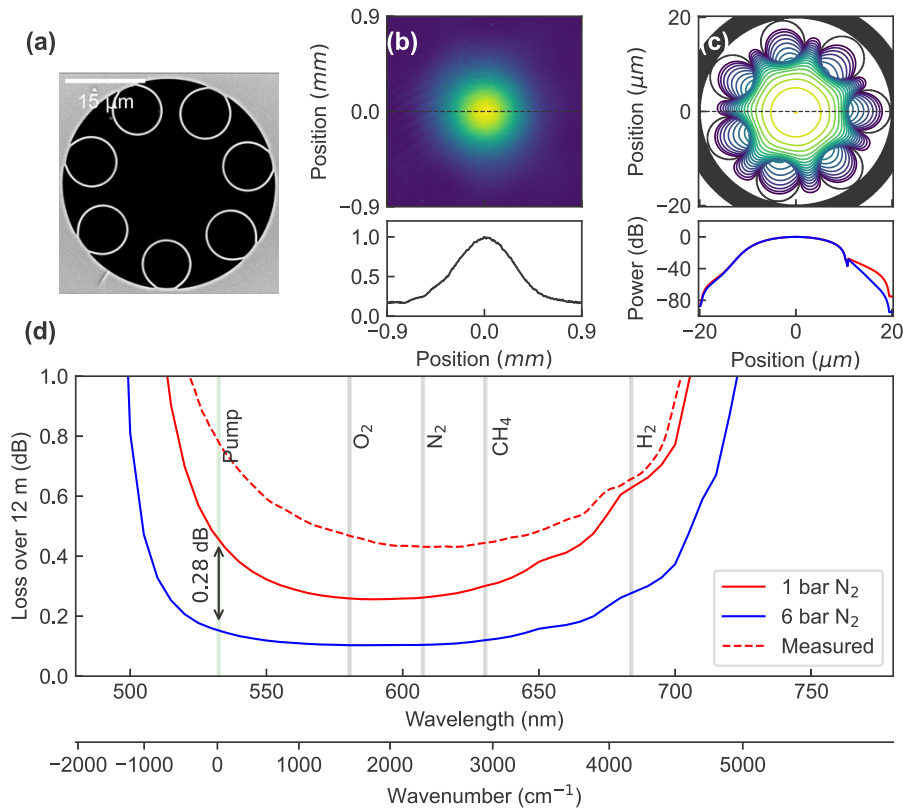
Fig. 2. (a) SEM image of the fiber cross section. (b) Far field image of the fiber's fundamental mode adapted from [28]. The lower panel shows the cross-sectional intensity profile (c) 3-dB contour plot of fundamental mode's z-Poynting vector from modelling. The lower panel shows cross sectional profiles of the normalized power considering the core filled with 1 bar nitrogen (red) and 6 bar nitrogen (blue). (d) Simulated loss in the visible over 12 m of fiber for the core filled with 1 bar nitrogen (red) and the inlet set to 6 bar (blue) thus establishing a pressure profile along the fiber. The dashed line is the experimentally measured loss. Note that microbending contributions (which increases with decreasing wavelength) to the loss were neglected from the simulations, meaning that the disagreement with the experimentally measured loss becomes more apparent going towards the short wavelength edge. Some additional macrobend loss will contribute to this also.

when the core and cladding are both at atmospheric pressure is shown by the dashed red curve [28]. Note that the bandwidth is sufficient to accommodate the pump at 532 nm, and several Stokes shifts for different gas species up to vibrational hydrogen at 683 nm [8]. Raising the core pressure increases the bandwidth and reduces loss (by 0.28 dB at 532 nm), improving the system performance across the entire spectral gas range.

To further illustrate this concept in terms of the Raman capture efficiency, we can define quantity known as the effective fiber interaction length L_{eff} [31]

$$L_{\text{eff}} = \int_0^L T_p(z)T_r(z)dz,\tag{1}$$

where for a back-scatter configuration, $T_p(z)$ is a function that represents the ratio of the pump power at a point z along the fiber to the total power coupled into the fiber and $T_r(z)$ is a function that represents the ratio of the Raman power generated at the end of the fiber to the power generated at a point z along the fiber. These are both in the form

$$T_p(z) = e^{-\alpha_p z}; \qquad T_r(z) = e^{-\alpha_r z},\tag{2}$$

where α_p is the fiber loss at the pump wavelength, and α_r the loss at the Stokes wavelength. Integrating over the fiber length L yields the following expression for L_{eff}

$$L_{\text{eff}} = \frac{1 - e^{-(\alpha_p + \alpha_r)L}}{\alpha_p + \alpha_r}.\tag{3}$$

The value of L_{eff} is strongly dependent on the fiber properties, and therefore the choice of filling scheme implemented in this work. Considering that the trace gases measured are in a nitrogen balance, and that by selectively filling the core of the fiber we raise the effective index of the fundamental mode at both the pump and Stokes wavelengths thereby reducing α_p and α_r, we would expect to increase the effective interaction length for our 12 m length of fiber.

Various values of α_p and α_r were calculated considering elevated nitrogen pressures in the core of the fiber (cladding tubes at atmospheric pressure). Note that in this case, we consider a flat pressure profile along the core, experimentally this would be non-uniform. This was done using Comsol Multiphysics, a commercial finite element solver, the simulated geometry obtained from the SEM image of the tubular fiber cross section shown in Fig. 1. The confinement loss for the fundamental mode was obtained from the imaginary part of the effective index, calculated at 532 nm and 630 nm corresponding to the pump wavelength and methane Stokes shift respectively. L_{eff} is plotted against absolute core pressure in Fig. 3 and clearly shows a substantial increase in the fiber interaction length of approximately 2.5 m at 6 bar pressure (used in this work) compared to 1 bar pressure. Note that this simulation only considers the reduction in the confinement loss of the fundamental core mode. The GDRI effect reduces the loss of higher order core-guided modes as well [29] although they remain typically 10-200 times greater than for the fundamental mode. A reduction in loss of the higher order modes should also act to increase the effective numerical aperture of the fiber and thus the fiber's capture efficiency. While simulating the impact of this is somewhat more involved than the confinement loss reduction presented here, it is worth noting that experimentally we would expect a more significant improvement in LoD due to GDRI.
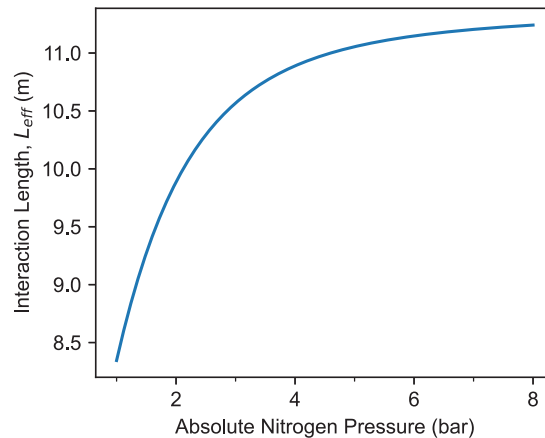
Fig. 3. Effective fiber interaction length plotted against absolute nitrogen pressure in the core.

4.   Results and discussion

4.1. Spectra

The selectivity and sensitivity of the system was evaluated by measuring trace quantities of methane and hydrogen loaded into the fiber at 5 bar gauge pressure. Figure 4 shows the resulting Raman spectra collected at concentrations of: (a) 100 ppm methane, 100 ppm hydrogen; (b) 20 ppm methane, 50 ppm hydrogen; (c) 5 ppm methane, 10 ppm hydrogen, all obtained with an integration time of 60 s. The red spectra were taken when pressurising both the core and cladding tubes, and the blue spectra when selectively filling the core with the gas sample. A noticeable increase in Raman signal strength is evident with the latter because of the GDRI effect. For all the blue spectra, two prominent vibrational peaks for CH_4 are visible at $2913 \, cm^{-1}$ and $3012 \, cm^{-1}$ which are associated with vibrations ν_1 and ν_3 respectively [8]. The highest intensity rotational-vibrational Q(1) peak for hydrogen is visible at $4153 \, cm^{-1}$ for all concentrations. Furthermore two additional peaks are just visible to the lower wavenumber side of Q(1), albeit at low resolution (see Fig. 4(a)) corresponding to additional vibrational-rotational Raman transitions Q(2) & Q(3) visible at $4146 \, cm^{-1}$ and $4126 \, cm^{-1}$ respectively which is consistent with previous works [19].

The linearity of the system was demonstrated by registering the methane and hydrogen peak height for varying concentrations ranging from 5–100 ppm. The fiber was flushed through with nitrogen prior to measuring each concentration. The results are shown in Fig. 5(a) and (b) and confirm a linear response for methane and hydrogen respectively at trace concentrations. For methane in Fig. 5(a), the ratio of the blue to the red curve is approximately 1.9, demonstrating that selectively filling the core and the associated improvement in the fiber's optical properties, including loss, that results, enable an increase in the captured and delivered Raman signal.

4.2. Fill time

For any gas sensor, a key parameter is the sensor response time. For HCFs, a significant part of the response time will be the time taken to fill the fiber with the gas sample. For this work, we use pressure-driven gas flow, enabled by the pressure differential between the gas inlet (at a gauge pressure of 5 bar) and the outlet (at atmospheric pressure). This pressure-driven gas flow is significantly faster than a purely diffusion-based method [32].
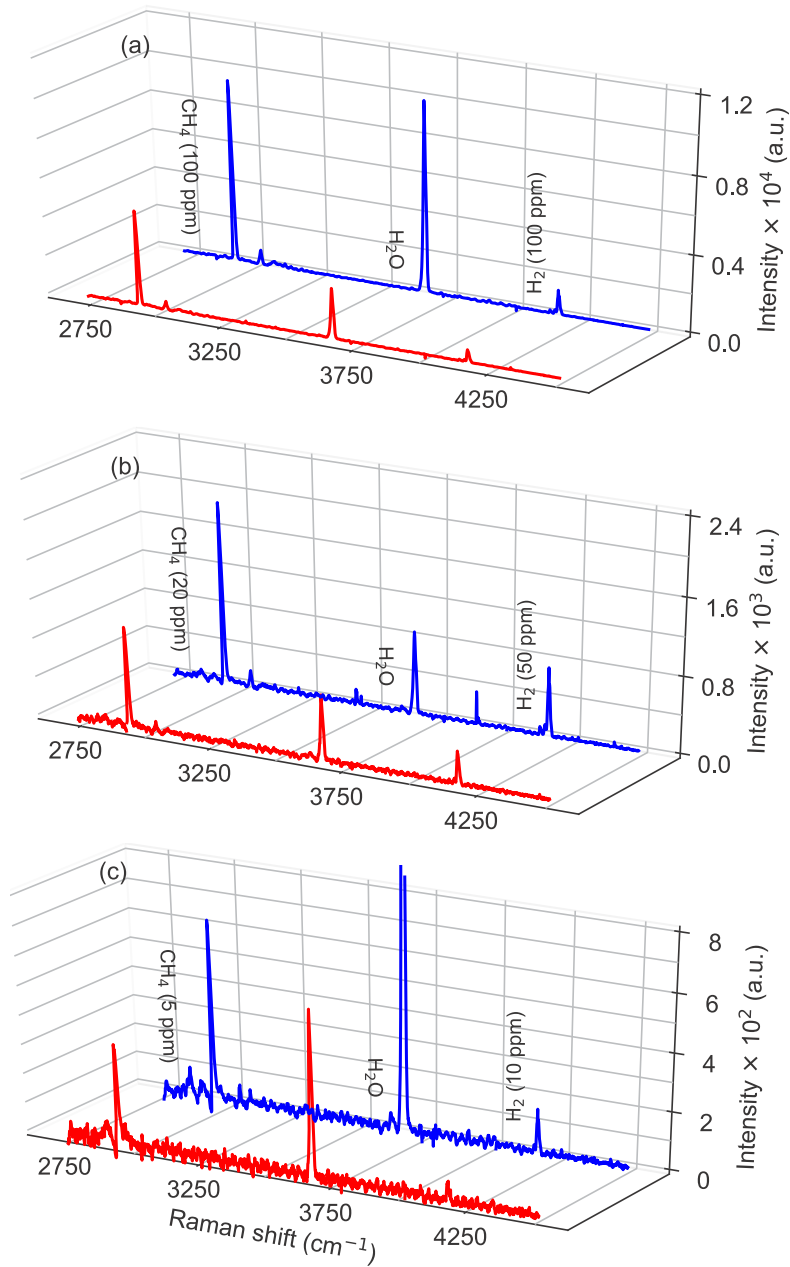
Fig. 4. Measured spectra of methane and hydrogen at varying concentrations within a 12 m length of HC-ARF with sealed cladding tubes (blue traces) and open cladding tubes (red traces) at the distal end. A series of 10 spectra is averaged, integration time 60 s. Spectrum of: (a) 100 ppm methane 100 ppm hydrogen; (b) 20 ppm methane 50 ppm hydrogen; (c) 5 ppm methane and 10 ppm hydrogen.
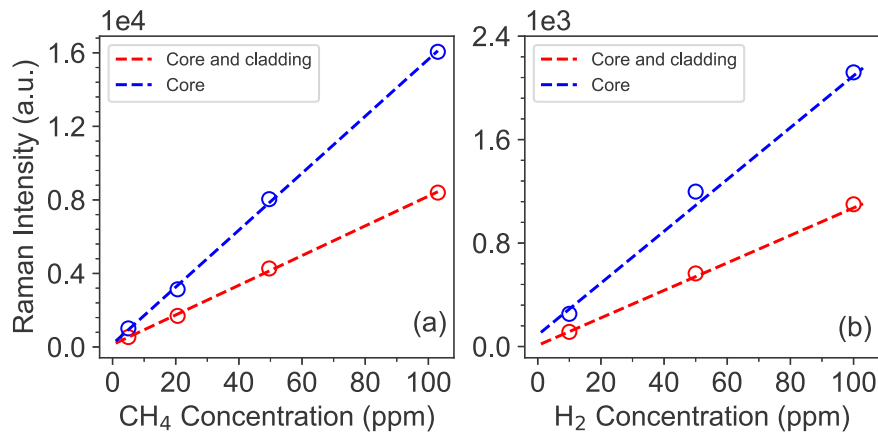
Fig. 5. Linearity of signal with concentration (determined from peak height) for methane on the right, and hydrogen on the left within a 12 m length of fiber with sealed cladding tubes (blue traces) and open cladding tubes (red traces) at the distal end. A series of 10 spectra is averaged, acquisition time 60 s, filling pressure 5 bar.

To evaluate the gas filling time, we first filled our 12 m fiber, with both core and cladding elements open, from the distal end with 100 ppm methane at a gauge pressure of 5 bar and recorded the methane ν_1 vibrational band peak integral every 2 s. The results are shown in Fig. 6(a) where a Savitzky Golay filter (solid red line) has been applied to the raw data (grey circles). Initially the Raman signal increases, until after $\sim$ 241 s when it slowly decays, reaching a steady state after $\sim$ 764 s. In all previous work, the filling time of HCFs has been discussed in the context of how long the core region takes to fill with the gas sample. However, this behavior in Fig. 6(a) can be explained using the GDRI effect; due to the different core and cladding tube diameters, the hollow core and the cladding tubes of the microstructure reach a steady state pressure at different rates. While the core and cladding elements contain gas at different pressures, there is a transient differential pressure between these regions which leads to a GDRI and transient changes in the optical properties of the fiber. For this reason, the response time of the system is not only dictated by the time to fill the core, but also the surrounding capillaries, and given that the radius of the surrounding capillaries is around half that of the core, there is an approximately four-fold increase in the fill time, t_f, since for a circular bore $t_f \propto 1/r^2$ [33]. We would expect the gas flow dynamics to differ slightly experimentally due to the non-circular core boundary. Note that the fill time of the cladding elements of the HC-ARF is important in all gas-filling applications of HC-ARFs, not just the Raman gas sensing application described here.

Next, we investigated the gas filling time for selective core filling (i.e. with the cladding holes sealed as described in Section 2.2). The results of this filling scheme are shown in Fig. 6(b). Here, the fill time, $t_f t_f$ is defined as the time taken to reach 90% of the applied concentration (103 ppm), which is 283 s in this case, significantly shorter than the previous method. Also, the Raman signal plateaus as expected without any subsequent decay

4.3. Limit of detection

To determine the minimum detection limit of the two filling schemes for methane, the fiber was filled with 100 ppm methane balanced in nitrogen. To evaluate the long-term stability and precision of the system an Allan-Werle deviation calculation was carried out by continuously measuring the main methane symmetric stretch band (ν_1) over a time of 1 hour. For a time-series data $y(t)$ separated into M blocks each of time length $\tau = n\tau_0$, with n being an integer, and $\tau_0 = 2$
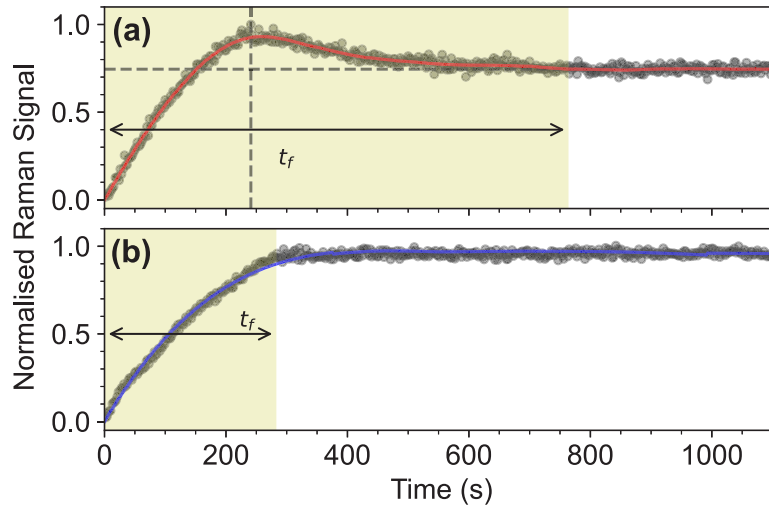
Fig. 6. Continuous monitoring of the Raman signal when filling with 100 ppm methane (2 s acquisition time). (a) Evolution of methane Raman signal with time when gas is loaded into both the core and cladding of the fiber. The Raman signal exhibits a transient response increasing, reaching a maximum then gradually settling down to a steady state. The signal reaches a steady state after t_f ~ 764 s. (b) As in (a) but loading the gas selectively into the fiber core, the signal reaches a steady state after t_f ~ 283 s.

s being the integration time the set of M data were acquired with, the Allan deviation $\sigma_y(\tau)$ is calculated by

$$\sigma_y(\tau) = \sqrt{\frac{1}{2(M-1)} \sum_{k=1}^{M-1} (\bar{y}_{k+1} - \bar{y}_k)^2}, \tag{4}$$

where $\bar{y}_k$ denotes the average of the kth block.

The Allan deviation for this gas mixture for both gas filling schemes is shown in Fig. 7. Initially, both curves follow a ~ $1/\sqrt{\tau}$ trend, with τ being the integration time, associated with CCD read-out noise. Beyond this, thermal mechanical drift begins to take effect. For 100 s integration, the minimum detection limit indicated in Fig. 7(a) is ~0.7 ppm and for (b) ~ 0.36 ppm. For Fig. 7(b) the Allan-deviation at 10 s integration time was ~1 ppm, dropping well below 1 ppm at ~20 s and then reducing to ~0.15 ppm at ~200 s. Longer integration times up to ~600 s (optimum integration time) allow for a lower LoD. This clearly demonstrates that this system is capable of a sub-ppm methane measurement given sufficient integration time of 20 s or more and demonstrates significant improvement with the selective core filling scheme.
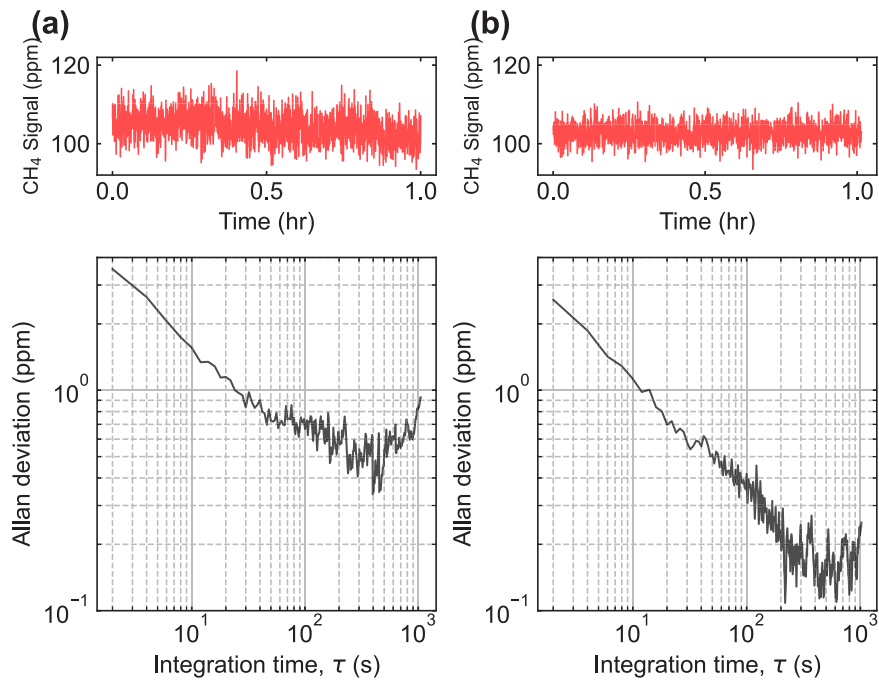
Fig. 7. Allan-Werle plots for open (a) and sealed cladding tubes (b) obtained from the measurement of a 100 ppm CH_4 calibration gas mixture (upper plots) over a period of one hour.

5. Conclusion

The HC-ARF used here has a sufficiently low loss and broad spectral range to detect both CH_4 and H_2 simultaneously as well as N_2 and O_2. Detection of these gases in trace concentrations has applications in biomedical fields, for example with breath analysis where hydrogen and methane biomarkers can be used to diagnose malabsorption disorders. Of course, the technique is not restricted to the aforementioned homonuclear diatomic gases, the emphasis being that the monitoring of multiple homonuclear species at low concentrations is difficult using conventional techniques. We demonstrate that there is good signal linearity for both CH_4 and H_2, even down to low concentrations which is useful for quantification analysis. We have also demonstrated, for the first time, that changes in the fiber's optical properties due to differential gas pressure (and subsequently differential refractive index) between the core and cladding regions of the HC-ARF can be exploited, along with longer fiber lengths, to improve the LoD and gas filling time (and thus overall sensor response time). By loading the gas sample only into the core and subsequently raising the core pressure above that of the surrounding capillaries which are at atmospheric pressure, not only is the response time substantially reduced (factor of ∼3), but the impact on the fiber's optical properties also leads to an increase in the observed Raman signal, by almost a factor of 2 here further reducing the sensitivity to 0.15 ppm for methane gas with a low power pump source, below that of 0.2 ppm demonstrated using a PBGF at significantly higher gas pressure and pump power [19]. To further exploit the low loss of the fiber, with the aid of non-invasive femto-second laser machining to drill side-channels through the fiber jacket to selectively access the fiber core as opposed to sealing the capillaries, the gas filling time bottleneck could be addressed, allowing significantly longer lengths of fiber to be used, further reducing the LoD [34]. In-line natural gas monitoring (propane, methane and butane)

could be a practical application for the proposed system. Potentially, such a fiber-based system could measure highly pressurised gases without requiring any pressure reduction stages, while of course benefiting from the improvement in fiber performance.

Disclosures. The authors declare that there are no conflicts of interest related to this article.

Data availability. All data supporting this study are available from the University of Southampton repository at [35].

References

1. F. Caldararu, C. Ionescu, A. Vasile, and M. Caldararu, "Chemo-optical sensor for toxic gases detection," in *The 28th International Spring Seminar on Electronics Technology: Meeting the Challenges of Electronics Technology Progress* (2005).
2. J. R. Stetter and J. Ling, "Amperometric Gas Sensors - A Review," Chem. Rev. **108**(2), 352–366 (2008).
3. C. Deng, J. Zhang, X. Yu, W. Zhang, and X. Zhang, "Determination of acetone in human breath by gas chromatography–mass spectrometry and solid-phase microextraction with on-fiber derivatization," J. Chromatogr. B: Anal. Technol. Biomed. Life Sci. **810**(2), 269–275 (2004).
4. A. Sepman, Y. Ögren, Z. Qu, H. Wiinikka, and F. M. Schmidt, "Tunable Diode Laser Absorption Spectroscopy Diagnostics of Potassium, Carbon Monoxide, and Soot in Oxygen-Enriched Biomass Combustion Close to Stoichiometry," Energy Fuels **33**(11), 11795–11803 (2019).
5. S. Hammer, D. W. T. Griffith, G. Konrad, S. Vardag, C. Caldow, and I. Levin, "Assessment of a multi-species in situ FTIR for precise atmospheric greenhouse gas observations," Atmos. Meas. Tech. **6**(5), 1153–1170 (2013).
6. R. J. Westerwaal, S. Gersen, P. Ngene, H. Darmeveil, H. Schreuders, J. Middelkoop, and B. Dam, "Fiber optic hydrogen sensor for a continuously monitoring of the partial hydrogen pressure in the natural gas grid," Sens. Actuators, B **199**, 127–132 (2014).
7. M. Aker, K. Altenmüller, and A. Beglarian, *et al.*, "Quantitative Long-Term Monitoring of the Circulating Gases in the KATRIN Experiment Using Raman Spectroscopy," Sensors **20**(17), 4827 (2020).
8. W. R. Fenner, H. A. Hyatt, J. M. Kellam, and S. P. S. Porto, "Raman cross section of some simple gases," J. Opt. Soc. Am. **63**(1), 73–77 (1973).
9. M. Hippler, "Cavity-Enhanced Raman Spectroscopy of Natural Gas with Optical Feedback cw-Diode Lasers," Anal. Chem. **87**(15), 7803–7809 (2015).
10. P. Wang, W. Chen, J. Wang, F. Zhou, J. Hu, Z. Zhang, and F. Wan, "Hazardous Gas Detection by Cavity-Enhanced Raman Spectroscopy for Environmental Safety Monitoring," Anal. Chem. **93**(46), 15474–15481 (2021).
11. M. Nikodem, "Laser-Based Trace Gas Detection inside Hollow-Core Fibers: A Review," Materials **13**(18), 3983–4001 (2020).
12. P. Zhao, Y. Zhao, H. Bao, H. L. Ho, W. Jin, S. Fan, S. Gao, Y. Wang, and P. Wang, "Mode-phase-difference photothermal spectroscopy for gas detection with an anti-resonant hollow-core optical fiber," Nat. Commun. **11**(1), 847 (2020).
13. P. Zhao, H. L. Ho, W. Jin, S. Fan, S. Gao, Y. Wang, and P. Wang, "Gas sensing with mode-phase-difference photothermal spectroscopy assisted by a long period grating in a dual-mode negative-curvature hollow-core optical fiber," Opt. Lett. **45**(20), 5660–5663 (2020).
14. Y. Zhao, Y. Qi, H. L. Ho, S. Gao, Y. Wang, and W. Jin, "Photoacoustic Brillouin spectroscopy of gas-filled anti-resonant hollow-core optical fibers," Optica **8**(4), 532–538 (2021).
15. P. Jaworski, K. Krzempek, P. Kozioł, D. Wu, F. Yu, P. Bojęś, G. Dudzik, M. Liao, J. Knight, and K. Abramski, "Sub parts-per-billion detection of ethane in a 30-meters long mid-IR Antiresonant Hollow-Core Fiber," Opt. Laser Technol. **147**, 107638 (2022).
16. M. P. Buric, K. P. Chen, J. Falk, and S. D. Woodruff, "Enhanced spontaneous Raman scattering and gas composition analysis using a photonic crystal fiber," Appl. Opt. **47**(23), 4255–4261 (2008).
17. M. P. Buric, K. P. Chen, J. Falk, and S. D. Woodruff, "Improved sensitivity gas detection by spontaneous Raman scattering," Appl. Opt. **48**(22), 4424–4429 (2009).
18. S. Hanf, T. Bögözi, R. Keiner, T. Frosch, and J. Popp, "Fast and Highly Sensitive Fiber-Enhanced Raman Spectroscopic Monitoring of Molecular H2 and CH4 for Point-of-Care Diagnosis of Malabsorption Disorders in Exhaled Human Breath," Anal. Chem. **87**(2), 982–988 (2015).
19. S. Hanf, R. Keiner, D. Yan, J. Popp, and T. Frosch, "Fiber-Enhanced Raman Multigas Spectroscopy: A Versatile Tool for Environmental Gas Sensing and Breath Analysis," Anal. Chem. **86**(11), 5278–5285 (2014).
20. K. K. Chow, M. Short, S. Lam, A. McWilliams, and H. Zeng, "A Raman cell based on hollow core photonic crystal fiber for human breath analysis," Med. Phys. **41**(9), 092701 (2014).
21. D. Pryamikov, A. S. Biriukov, A. F. Kosolapov, V. G. Plotnichenko, S. L. Semjonov, and E. M. Dianov, "Demonstration of a waveguide regime for a silica hollow - core microstructured optical fiber with a negative curvature of the core boundary in the spectral region > 3.5 μm," Opt. Express **19**(2), 1441–1448 (2011).
22. F. Poletti, "Nested antiresonant nodeless hollow core fiber," Opt. Express **22**(20), 23807–23828 (2014).

23. W. Belardi and J. C. Knight, "Hollow antiresonant fibers with reduced attenuation," Opt. Lett. **39**(7), 1853–1856 (2014).

24. W. S. M. Brooks, M. Partridge, I. A. K. Davidson, C. Warren, G. Rushton, J. Large, M. Wharton, J. Storey, N. V. Wheeler, and M. J. Foster, "Development of a gas-phase Raman instrument using a hollow core anti-resonant tubular fiber," J. Raman Spectrosc. **52**(10), 1772–1782 (2021).

25. A. Knebl, R. Domes, D. Yan, J. Popp, S. Trumbore, and T. Frosch, "Fiber-Enhanced Raman Gas Spectroscopy for ^{18}O–^{13}C-Labeling Experiments," Anal. Chem. **91**(12), 7562–7569 (2019).

26. J. Wang, W. Chen, P. Wang, Z. Zhang, F. Wan, F. Zhou, R. Song, Y. Wang, and S. Gao, "Fiber-enhanced Raman spectroscopy for highly sensitive H_2 and SO_2 sensing with a hollow-core anti-resonant fiber," Opt. Express **29**(20), 32296–32311 (2021).

27. Thorlabs, "HC-532-01 HC-PBF datasheet," Microsoft Word - 040213 Master spec sheet HC-532-01.doc, Accessed 14/06, 2022.

28. I. A. Davidson, M. Partridge, J. R. Hayes, Y. Chen, T. D. Bradley, H. Sakr, S. Rikimi, G. T. Jasion, E. N. Fokoua, M. Petrovich, F. Poletti, D. J. Richardson, and N. V. Wheeler, "Tubular anti-resonant hollow core fiber for visible Raman spectroscopy," Proc. SPIE **11206**, 1120601 (2019).

29. T. W. Kelly, P. Horak, I. A. Davidson, M. Partridge, G. T. Jasion, S. Rikimi, A. Taranta, D. J. Richardson, F. Poletti, and N. V. Wheeler, "Gas-induced differential refractive index enhanced guidance in hollow-core optical fibers," Optica **8**(6), 916–920 (2021).

30. T. W. Kelly, I.A.K Davidson, S. Rikimi, G.T. Jasion, M.C. Partidge, W.S.M. Brooks, M.J. Foster, F. Poletti, D.J. Richardson, P. Horak, and N.V. Wheeler, "Impact of Pressure-Induced Differential Refractive Index in Raman Spectroscopy using Hollow-Core Fibres," in *Conference on Lasers and Electro-Optics Europe & European Quantum Electronics Conference*, (Optical Society of America, 2021), pp. 1.

31. R. Altkorn, M. D. Malinsky, R. P. Duyne, and I. Koev, "Intensity Considerations in Liquid Core Optical Fiber Raman Spectroscopy," Appl. Spectrosc. **55**(4), 373–381 (2001).

32. W. A. Challener, A. M. Kasten, F. Yu, G. Puc, and B. J. Mangan, "Dynamics of Trace Methane Diffusion/Flow Into Hollow Core Fiber Using Laser Absorption Spectroscopy," IEEE Sens. J. **21**(5), 6287–6292 (2021).

33. R. Wynne and B. Barabadi, "Gas-filling dynamics of a hollow-core photonic bandgap fiber for nonvacuum conditions," Appl. Opt. **54**(7), 1751–1757 (2015).

34. A. V. Brakel, C. Grivas, M. N. Petrovich, and D. J. Richardson, "Micro-channels machined in microstructured optical fibers by femtosecond laser," Opt. Express **15**(14), 8731–8736 (2007).

35. T. W. Kelly, I. A. Davidson, C. Warren, W. S. M. Brooks, M. J. Foster, F. Poletti, D. J. Richardson, P. Horak, and N. V. Wheeler, "Dataset for "Sub-ppm Gas Phase Raman Spectroscopy in an Anti-resonant Hollow Core Fiber"," University of Southampton (2022), https://doi.org/10.5258/SOTON/D2326.